Supporting Information for "Crustal structure of the Western U.S. from Rayleigh and Love wave amplification"

William Sturgeon[1], Ana M.G. Ferreira[1,2], Lewis Schardong[3], Augustin Marignier[1,4]

[1]Department of Earth Sciences, Faculty of Mathematical & Physical Sciences, University College London, WC1E 6BT, UK

[2]CERIS, Instituto Superior Técnico, Universidade de Lisboa, Av. Rovisco Pais 1, 1049-001 Lisboa, Portugal

[3]The Geological Survey of Israel, Jerusalem, Israel

[4]Mullard Space Science Laboratory, University College London, RH5 6NT, UK

Contents of this file

References

Chai, C., Ammon, C. J., Maceira, M., & Herrmann, R. B. (2015). Inverting interpolated receiver functions with surface wave dispersion and gravity: Application to the western us and adjacent canada and mexico. *Geophysical Research Letters*, *42*(11), 4359–4366.

Crotwell, H. P., & Owens, T. J. (2005). Automated receiver function processing. *Seismological Research Letters*, *76*(6), 702–709.

Laske, G., Masters, G., Ma, Z., & Pasyanos, M. (2012). Crust1. 0: An updated global model of earth's crust. *Geophys Res Abs*, *14*, 3743.

Moschetti, M., Ritzwoller, M., Lin, F.-C., & Yang, Y. (2010). Crustal shear wave velocity structure of the western united states inferred from ambient seismic noise and earthquake data. *Journal of Geophysical Research: Solid Earth*, *115*(B10).

Porter, R., Liu, Y., & Holt, W. E. (2016). Lithospheric records of orogeny within the continental us. *Geophysical Research Letters*, *43*(1), 144–153.

Sambridge, M. (1999). Geophysical inversion with a neighbourhood algorithm—i. searching a parameter space. *Geophysical journal international*, *138*(2), 479–494.

Schardong, L., Ferreira, A. M., Berbellini, A., & Sturgeon, W. (2019). The anatomy of uppermost mantle shear-wave speed anomalies in the western us from surface-wave amplification. *Earth and Planetary Science Letters*, *528*, 115822.

Schmandt, B., Lin, F.-C., & Karlstrom, K. E. (2015). Distinct crustal isostasy trends east and west of the rocky mountain front. *Geophysical Research Letters*, *42*(23), 10–290.

Shen, W., & Ritzwoller, M. H. (2016). Crustal and uppermost mantle structure beneath the united states. *Journal of Geophysical Research: Solid Earth*, *121*(6), 4306–4342.

Xie, J., Chu, R., & Yang, Y. (2018). 3-d upper-mantle shear velocity model beneath the contiguous united states based on broadband surface wave from ambient seismic noise. *Pure and Applied Geophysics*, *175*(10), 3403–3418.

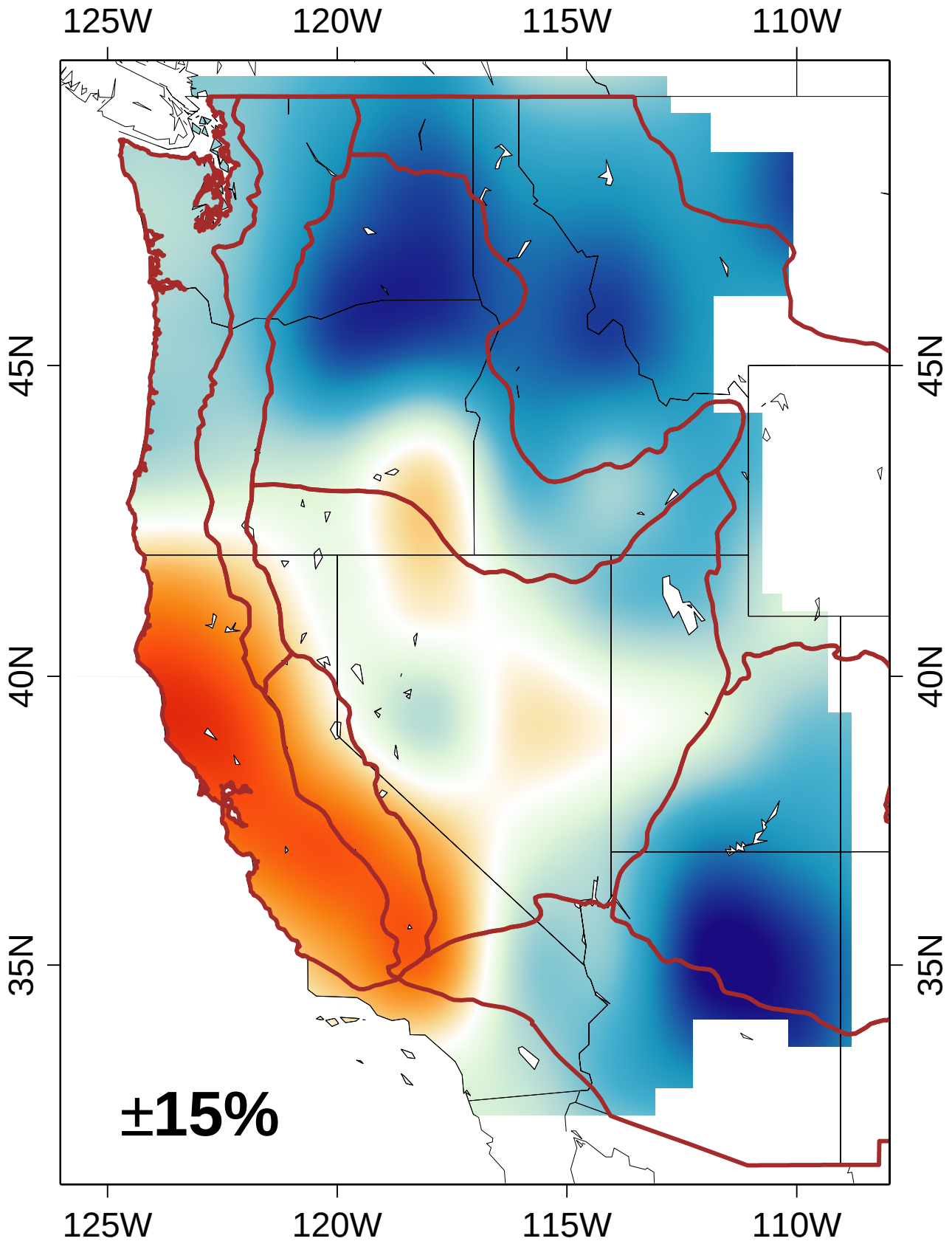

Figure S1. The crustal layer of SWUS-amp Schardong et al. (2019), shown in percentage perturbations from the averaged crustal v_S, where the maximum and minimum perturbations are 15%.

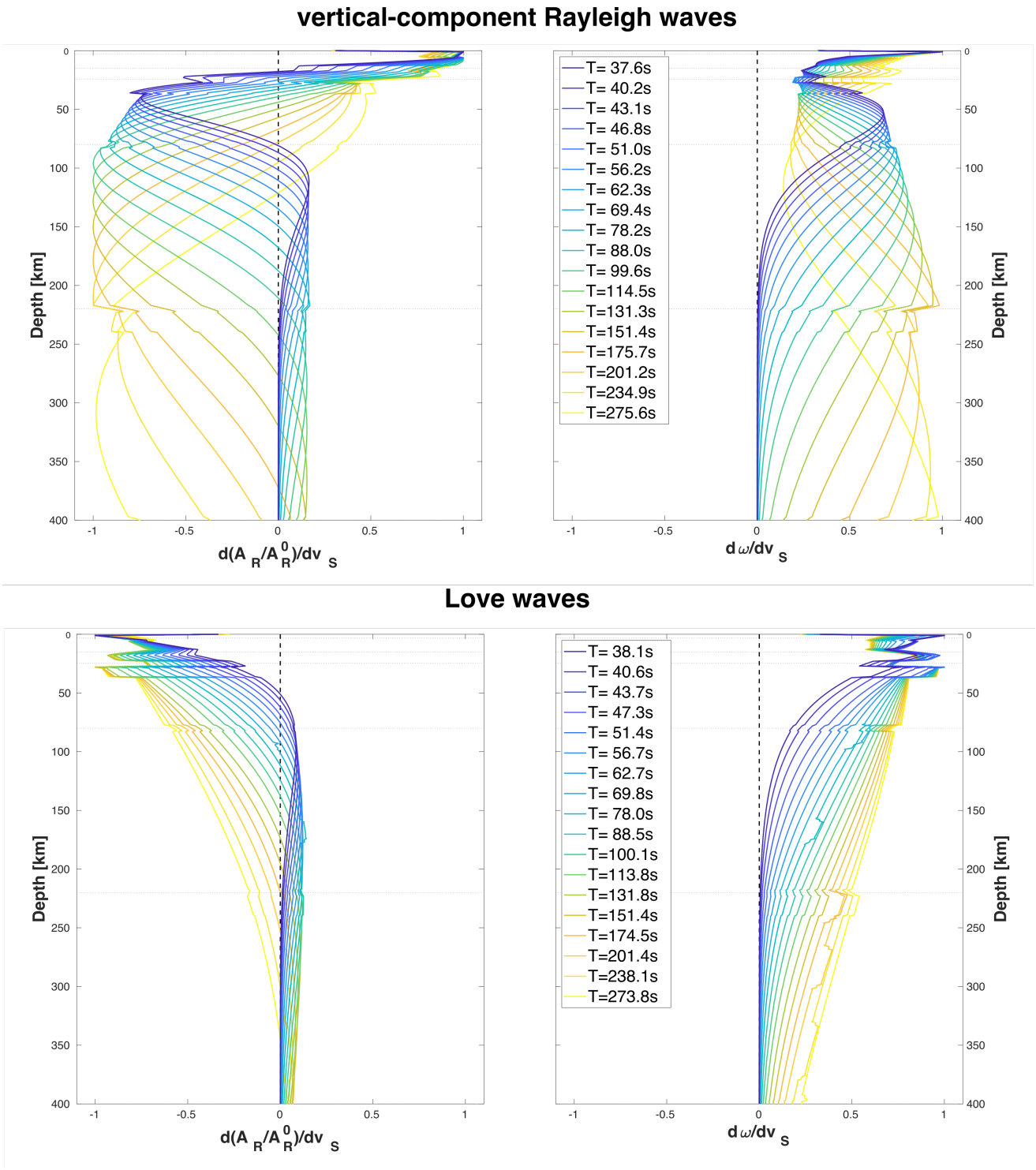

Figure S2. Sensitivity kernels of amplification (left) and phase velocity (right) to v_S for vertical-component Rayleigh waves (top row) and Love waves (bottom row) at all available periods.

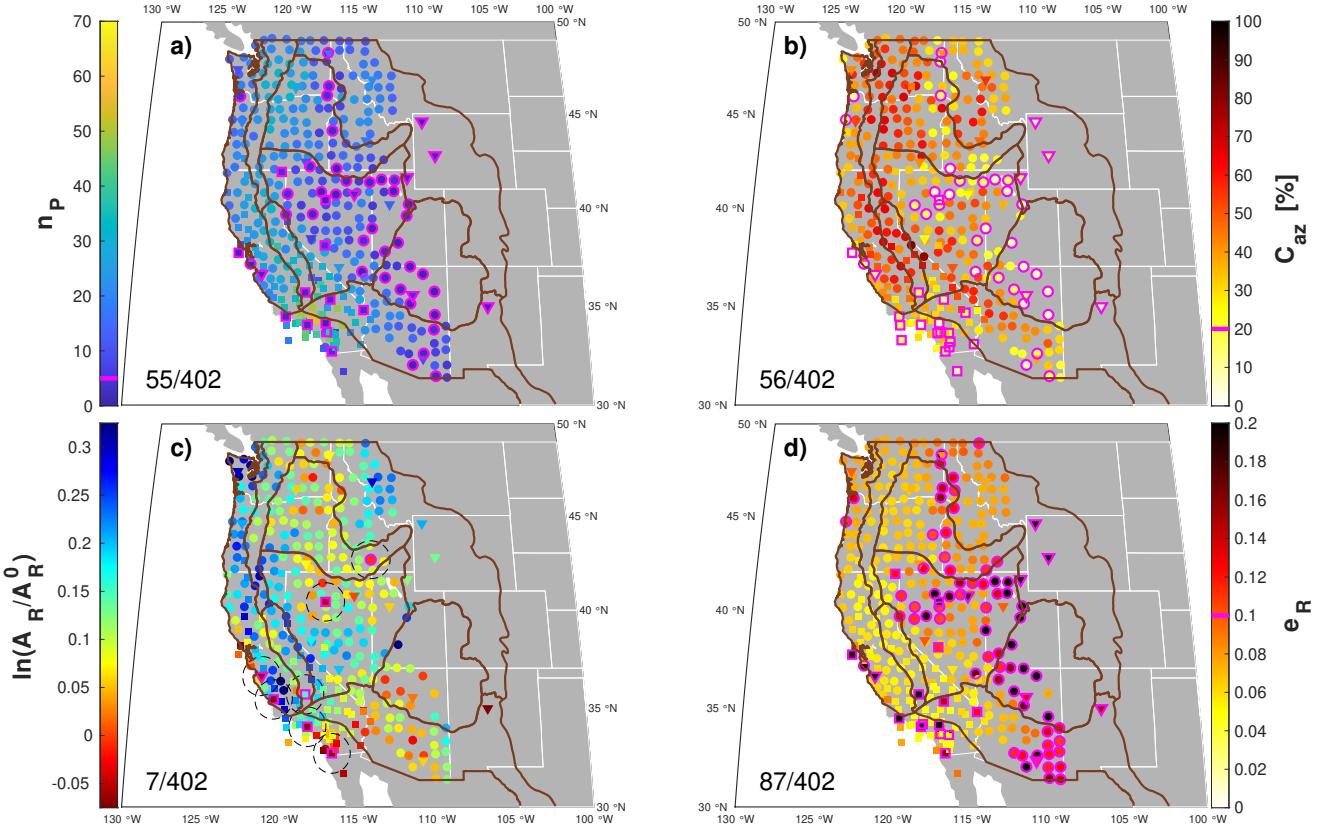

Figure S3. The selection process for fundamental mode Love wave local amplification at 38 s. From top-left to bottom-right, each sub-figure represents (a) selection upon the number of station pairs used to invert for local amplification at each receiver, (b) selection upon the azimuthal coverage of the station pairs used to invert for local amplification at each receiver, (c) elimination of outliers based on local geographical coherency, and (d) selection upon the error on amplification factors. Symbols outlined in magenta on the maps represent discarded stations (the number of discarded stations is shown in the numerator in the bottom-left corner of each sub-figure and the number in the denominator is the total number of stations), and magenta ticks on the colour bars represent the selection threshold when applicable.

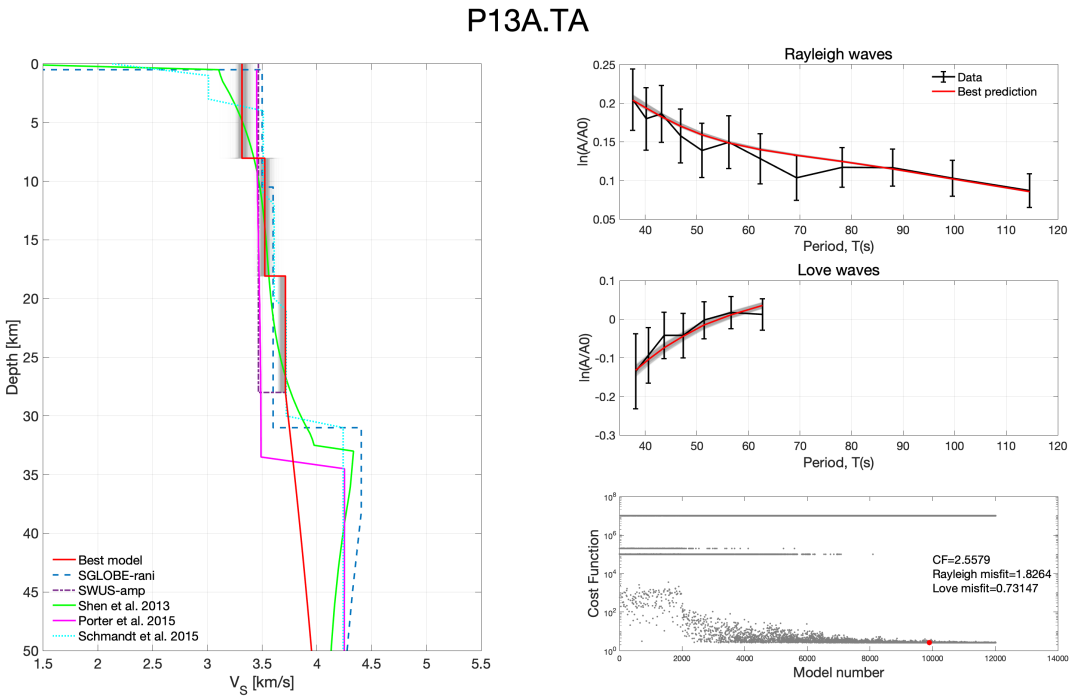

Figure S4. Example of an inversion using the Neighbourhood Algorithm (Sambridge, 1999) for stations P13A.TA. Left: 1D profile of V_S against depth for this study (red line) and other studies (coloured lines, as shown in legend). Top right: Rayleigh wave amplification curves. Middle right: Love wave amplification curves. Bottom right: cost-function evolution for the inversion, the red dot corresponds to the model with the lowest misfit.

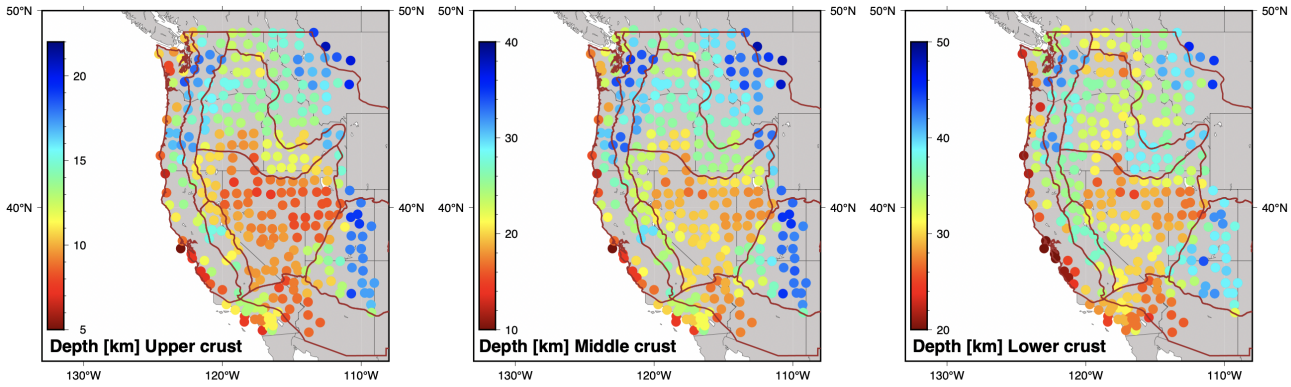

Figure S5. The depths of each crustal layer beneath each station used in this study. Depths are defined by those in CRUST1.0 (Laske et al., 2012)

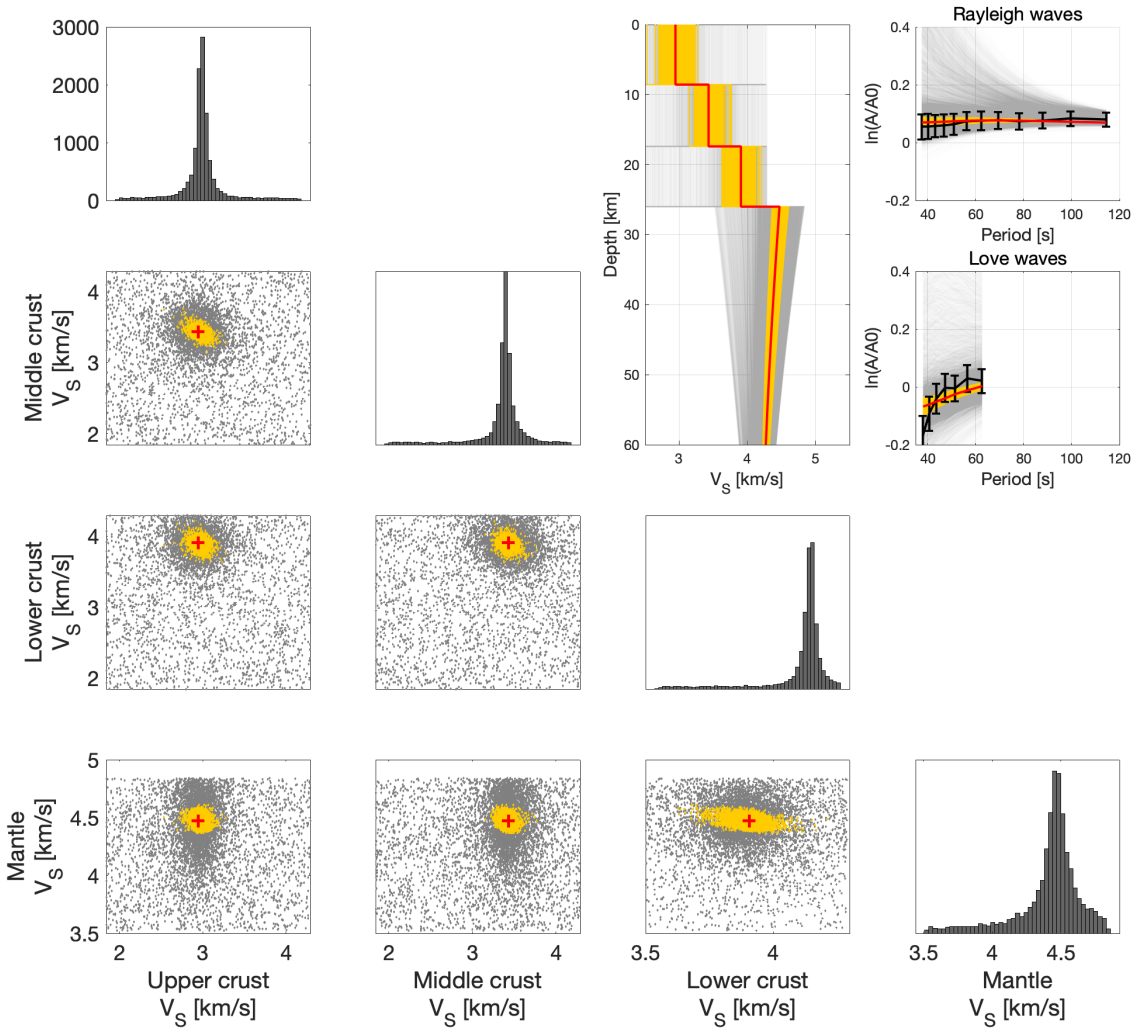

Figure S6. Example of parameter trade-offs for the station TA.Y13A. We show the trade-off in V_S for the upper crust, middle crust, lower crust, and uppermost mantle. The uppermost mantle is defined as being between the moho depth (35km) to ∼100 km. We perturb the uppermost mantle V_S using a single spline in this depth range. Histograms are also included for each parameter. Red lines and crosses represent the model with the lowest misfit, yellow lines and dots represent models with 20% of the best model and grey lines and dots represent all models search in the inversion.

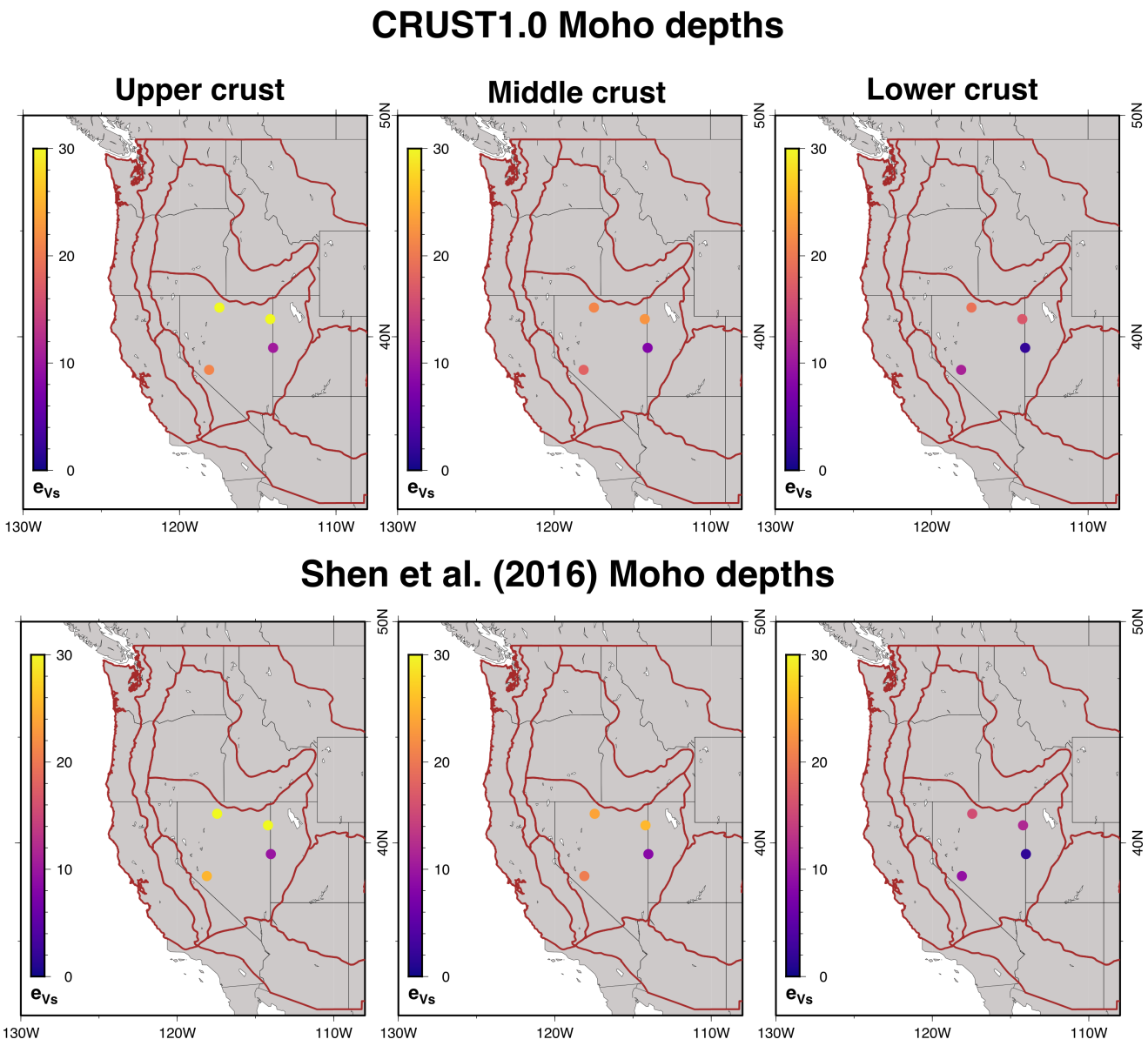

Figure S7. Uncertainty of station shear-wave velocity for four stations in the North Basin and Range, as given by Equation 8 in the main manuscript. Top row: Uncertainty of station velocity when defining the depth of each crustal layer using the model CRUST1.0 (Laske et al., 2012). Bottom row: the same as the top row but using the crustal depths from (Shen & Ritzwoller, 2016).

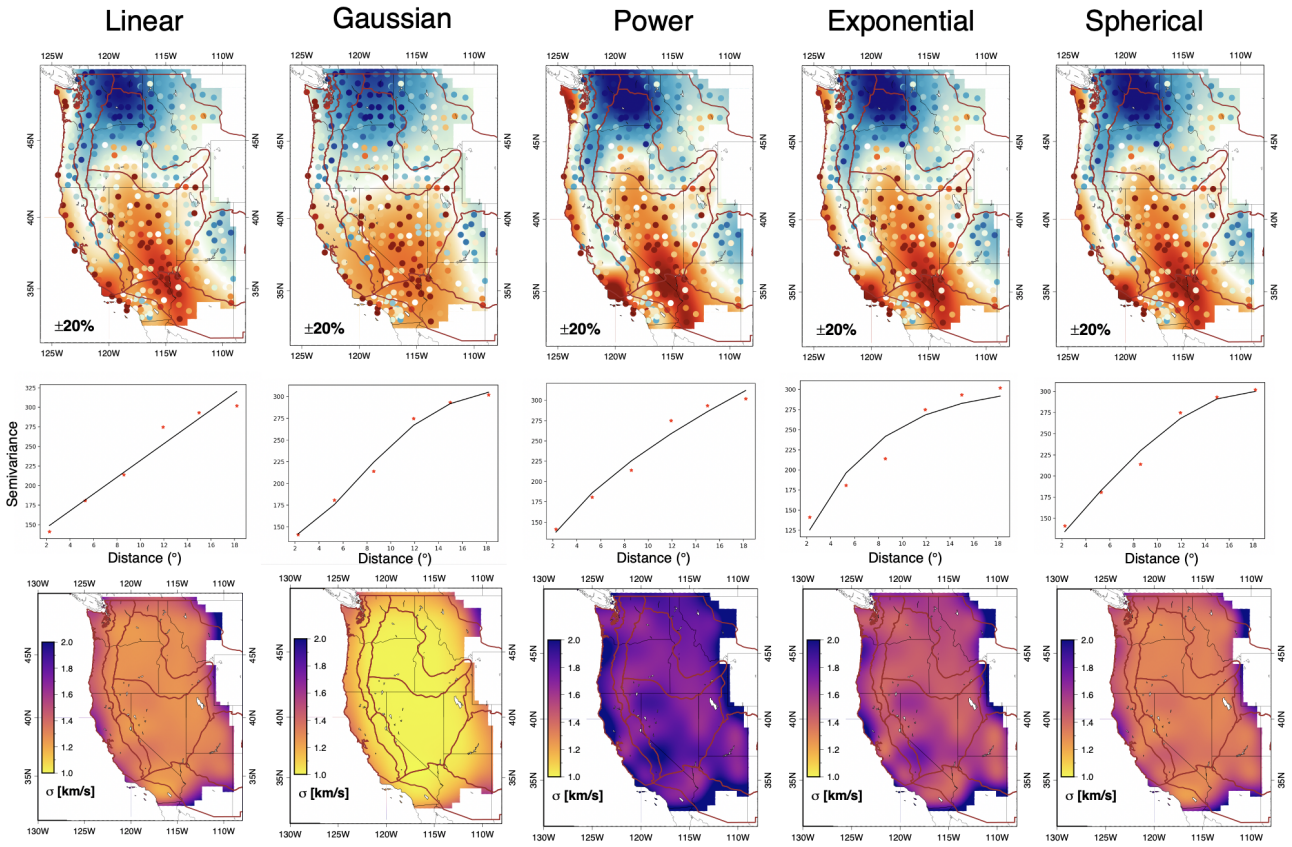

Figure S8. Ordinary kriging analysis in the upper crustal layer. We explore the effects of using a linear, gaussian, power, exponential and spherical model parameterisation to fit the semi-variogram. Top row: stations coloured by perturbations in v_S from the average v_S in the layer, and the interpolated map behind. Note the limits of the perturbations are given in the bottom left corner. Middle row: the respective semi-variograms. Bottom row: standard deviation of the kriging interpolation of perturbations of v_S from the average value in the layer.

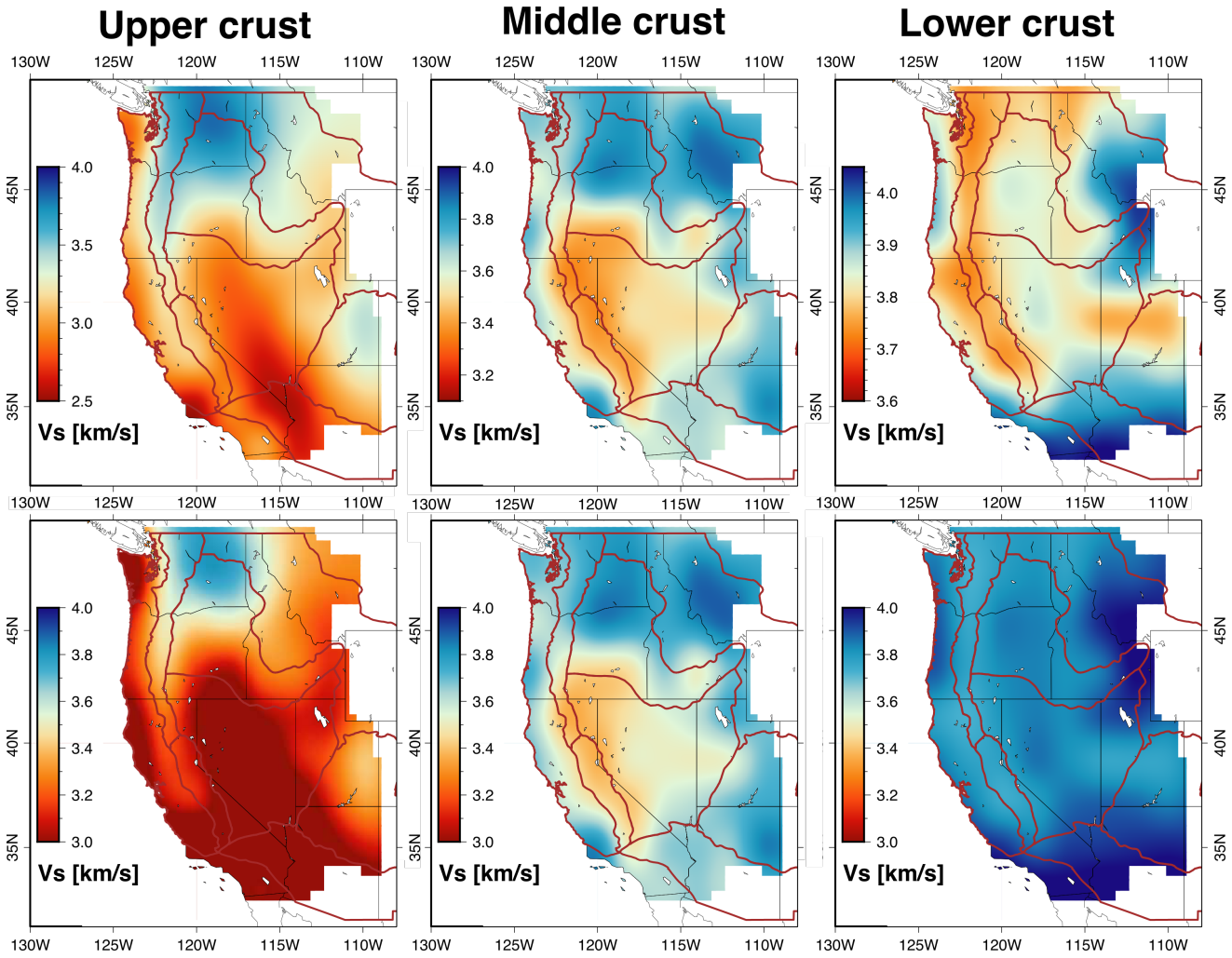

Figure S9. Top row: SWUS-crust absolute v_S plotted with different colour scales to further highlight the various features in the model. Bottom row: the same as the top row but with the scale fixed across all layers.

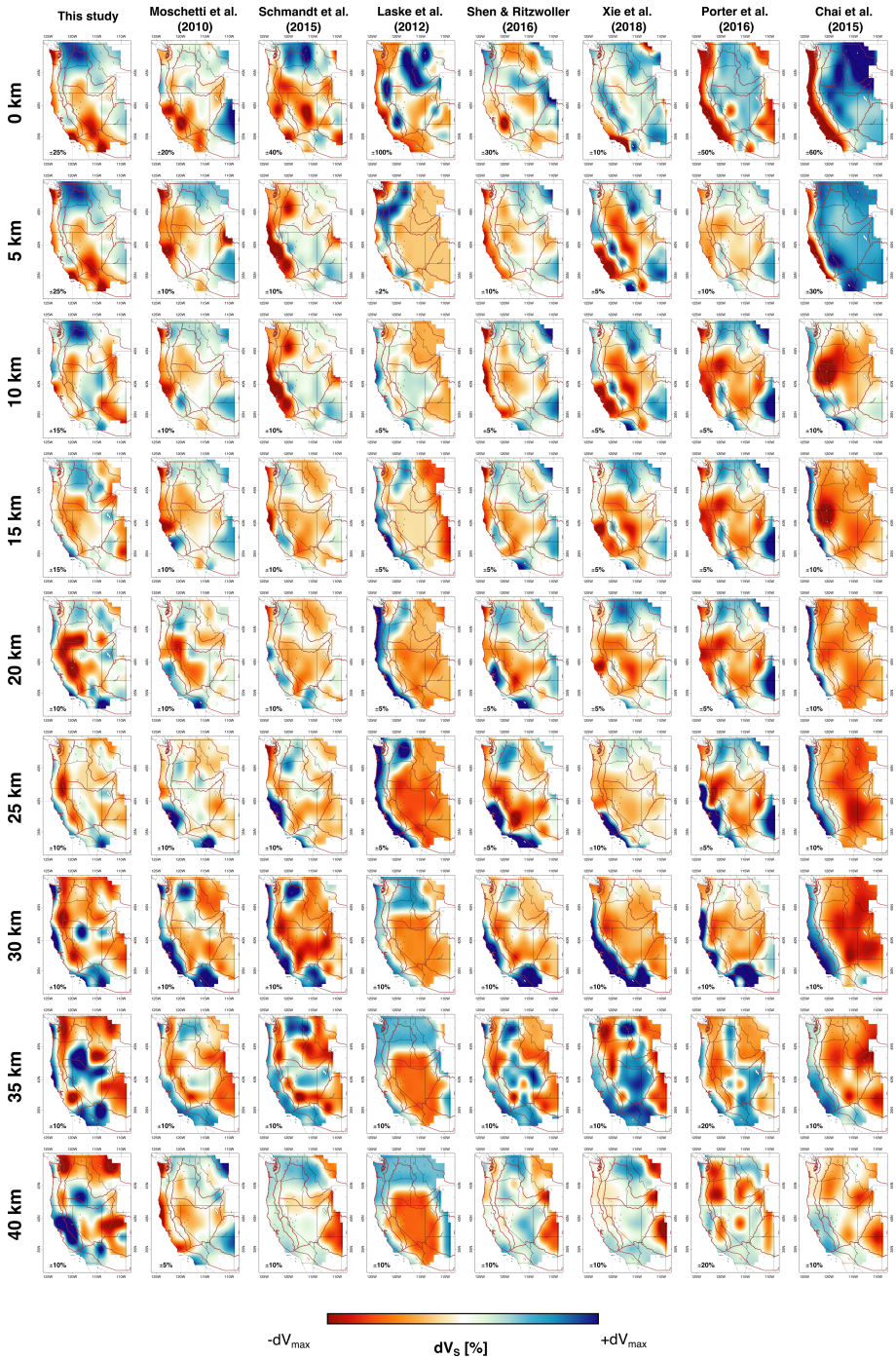

Figure S10. Comparison of the SWUS-crust v_S model (first column) with other local tomographic models Moschetti et al. (2010); Schmandt et al. (2015); Laske et al. (2012); Shen and Ritzwoller (2016); Xie et al. (2018); Porter et al. (2016); Chai et al. (2015) at crustal depths. The velocity perturbations of all models are expressed with respect to the average velocity at each depth respectively. The limits of the colour scale of each model and at each depth are displayed in the bottom left corner of each map. Boundaries of tectonic provinces are represented by solid light brown lines. The lateral extents of our model is also added to each model in order to aid in their comparisons.

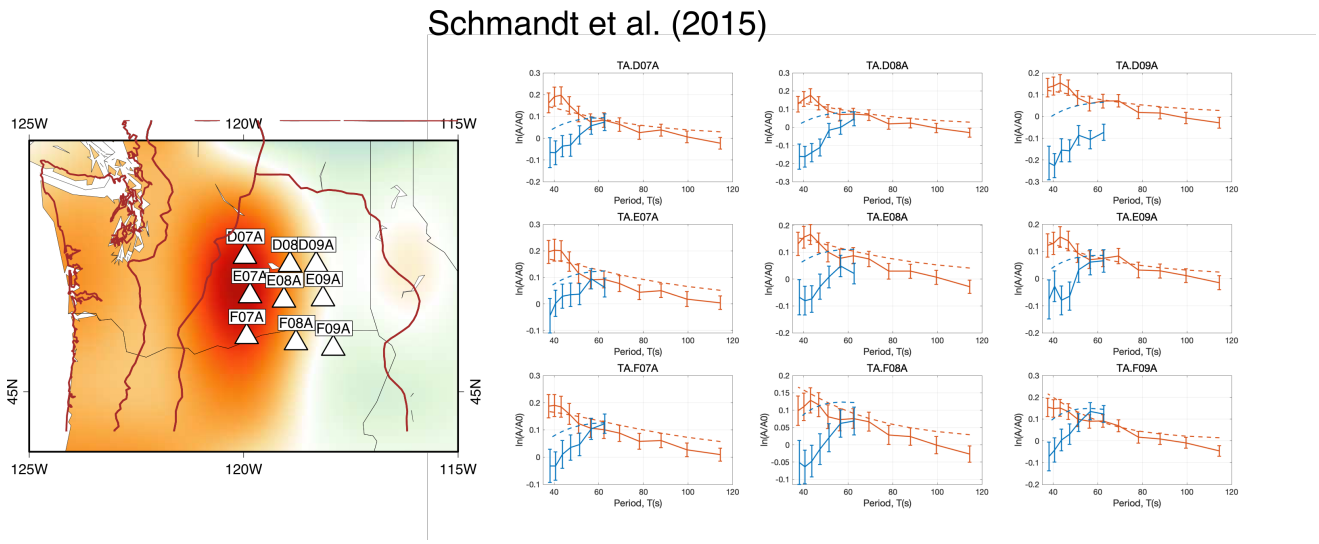

Figure S11. Prediction of amplification curves when using shear wave velocities from Shen and Ritzwoller (2016). Left: Map of Schmandt et al. (2015) in the upper crustal layer centred centred on the Columbia Basin and the location of the 9 stations used in this test. Right: Amplification curves for vertical-component Rayleigh waves (red curves) and Love waves (blue curves). The observed data are shown as solid lines with error bars, and the theoretical curves are shown as dashed lines.

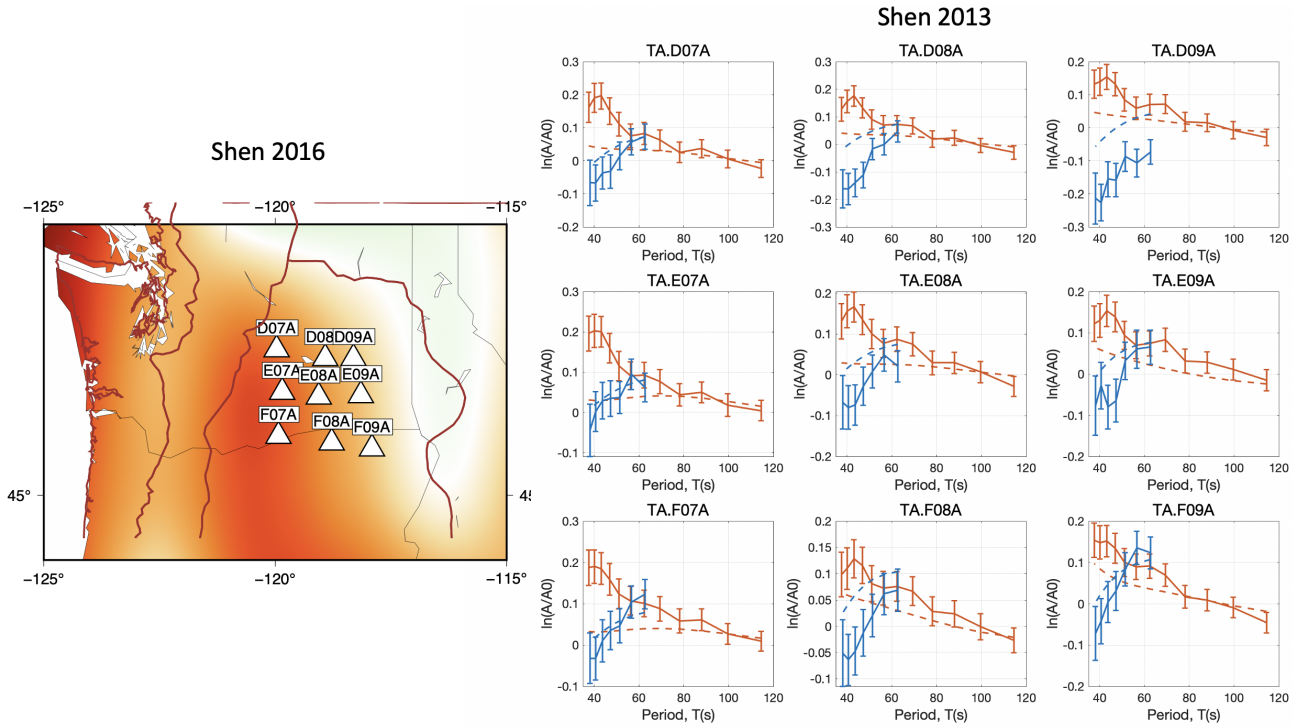

Figure S12. Prediction of amplification curves when using shear wave velocities from Shen and Ritzwoller (2016). Left: Map of Shen and Ritzwoller (2016) at 5 km depth centred on the Columbia Basin and the location of the 9 stations used in this test. Right: Amplification curves for vertical-component Rayleigh waves (red curves) and Love waves (blue curves). The observed data are shown as solid lines with error bars, and the theoretical curves are shown as dashed lines.

Table S1. Descriptions of the tomographic models analysed in this study.

Model	Datasets	Parameterisation		Forward modelling	3D inverse modelling & constraints
		Vertical	Horizontal		
CRUST1.0 (Laske et al., 2012)	Crustal thickness from active source seismic studies, receiver functions and gravity constraints v_s scaled from crustal types	Three crustal crystalline layers	1x1 degree cells	Compilation of existing datasets	
Moschetti et al. (2010)	Surface wave dispersion measurements from ambient seismic noise and teleseismic earthquakes (T 6-100s)	Three crustal layers	Interpolation of 1D profiles on 0.5° grid	Normal mode formalism	Monte Carlo inversion scheme Apriori v_P, v_S sediment and crustal thickness constraints
Schmandt et al. (2015)	Receiver functions Rayleigh wave phase velocity measurements (T 8-100 s) Rayleigh wave ellipticity maps (T 8-100s)	Three layered crust	Interpolated 1D profiles	Normal mode formalism?	Steepest descent No explicit regularisation
Shen and Ritzwoller (2016)	Rayleigh wave phase velocity measurements (T8-40 s, T28-80 s) Rayleigh wave group velocities (T8-28 s) Rayleigh wave ellipticity measurements (T 18-80s) Receiver functions	Four cubic B-splines	Kriging interpolation	Normal mode formalism?	.. Joint Bayesian Monte Carlo inversion Positive velocity jumps/gradients with depth Scaled v_P and density
Porter et al. (2016)	Rayleigh wave phase velocities (T 8-40 s) Wave gradiometry (T 20-150 s)	Crustal thickness estimates from the EarthScope Automated Receiver function Survey (EARS) Crotwell and Owens (2005)	0.25° grid	Normal mode formalism	Iterative linearised least squares inversion Damping applied
Xie et al. (2018)	Phase velocity measurements (T 10-150 s)	Four B-splines	Interpolation on 5° grid	Normal mode formalism	Non-linear MCMC inversion Increasing v_S with crustal depth
Chai et al. (2015)	Rayleigh wave group velocities (T 7-250 s) Bouger gravity observations P wave receiver functions	Smooth 1D profiles	1° cells	Finite difference approximations	Iterative linearised discrete inversion with smoothness-based stabilisation v_S increases with depth